M&C 2017 - International Conference on Mathematics & Computational Methods Applied to Nuclear Science & Engineering, Jeju, Korea, April 16-20, 2017, on USB (2017)

Demonstration of MAMMOTH Strongly-Coupled Multiphysics Simulation with the Godiva Benchmark Problem

Yaqi Wang,* Sebastian Schunert,* Javier Ortensi,† Frederick N. Gleicher,† Vincent M. Laboure,† Benjamin A. Baker,† Mark DeHart,† Richard C. Martineau,+

*Nuclear Engineering Method Development, Idaho National Laboratory, Idaho Falls, ID, USA
†Reactor Physics and Analysis, Idaho National Laboratory, Idaho Falls, ID, USA
+Modeling and Simulation, Idaho National Laboratory, Idaho Falls, ID, USA
yaqi.wang@inl.gov, sebastian.schunert@inl.gov, javier.ortensi@inl.gov, frederick.gleicher@inl.gov, vincent.laboure@inl.gov, benjamin.baker@inl.gov, mark.dehart@inl.gov, richard.martineau@inl.gov

Abstract - *This paper provides a detailed description of the Godiva benchmark problem suitable for multiphysics code verification. Multigroup transport weak forms for general curvilinear coordinates are derived using SAAF (self-adjoint angular flux) formulation. A new scheme based on spherical harmonics expansion for evaluating the angular derivative terms using the SN method are presented and tested. A one-dimensional spherical coordinate system is used by MAMMOTH for modeling the Godiva benchmark. Strongly-coupled multiphysics simulation mode of MAMMOTH is exercised and numerical results are given.*

I. INTRODUCTION

MAMMOTH is a MOOSE [1]-based nuclear reactor physics application developed at Idaho National Laboratory (INL). It performs tasks in a *multiphysics* environment ranging from detailed fuel-resolved analysis to full core reactor analysis by coupling other MOOSE-based applications including the radiation transport application Rattlesnake [2], the fuel performance application BISON [3] and the nuclear reactor system safety analysis application RELAP-7 [4], etc. MAMMOTH provides the linkage between various physics and radiation transport through multigroup cross sections. It can evaluate densities of stationary, diffusive or convective heavy metals and fission products. Verification and validation (V&V) of MAMMOTH is required in addition to the V&V of each individual dependent application. One way of doing this is by solving a set of well-defined benchmark problems.

The coupling through data transfer among participating applications has been demonstrated in previous work [5, 6, 7, 8]. In this pattern, all physics are modeled separately and the driving application is responsible for transferring the data to and from the other applications and converging them in a Picard iteration. All physics are solved independently one at a time. This coupling pattern is suitable for weakly coupled physics with significantly different time scales. On the other hand, MAMMOTH also allows strongly coupled multiphysics simulations with all physics residing in the same nonlinear system. All physics can be solved simultaneously in this coupling pattern. This paper exercises MAMMOTH with the Godiva benchmark problem in the strongly coupled multiphysics simulation mode.

Godiva [9, 10] is an unshielded bare spherical U-235 metal assembly originally situated at LANL in 1950s. The metal fuel assembly contains three sections fit together to form a sphere during an experiment. It has a critical mass of 54kg of uranium enriched to about 90% U-235 with a radius of 8.0725 cm. Two 7/16-inch-diameter uranium control rods with minimum reactivity insertion of 0.01 cents are used for controlling the assembly. The assembly becomes prompt super-critical initially by inserting the missing U-235 'button' into the sphere. The power quickly rises up from 1 watt to several gigawatts in a fraction of a millisecond. The power causes thermal expansion, increasing the neutron leakage and consequently making the assembly sub-critical, bringing its power down to a few megawatts.This quick thermal expansion causes the sphere to vibrate. Various researchers [11, 12] have used the Godiva benchmark to test their multiphysics calculations. Hence, it provides a perfect multiphysics benchmark problem for coupling neutronics and thermo-mechanics.

We first describe the Godiva benchmark abstracted from the experiment in detail in Section 2. We then present the neutron transport equation in the weak form with one-dimensional (1D) spherical coordinates used in Rattlesnake and the employed time integration scheme for solid mechanics. The numerical results along with the MAMMOTH settings are presented in Section 4. Finally, conclusions are drawn with regard to the multiphysics coupling.

II. DESCRIPTION OF THE GODIVA BENCHMARK PROBLEM

We first write down the governing equations with the examination of all the assumptions for the Godiva benchmark problem. Equations of conservation of momentum for solid-mechanics defined on the *reference* (un-deformed) solution domain $\mathcal{D}_0$ are:

$$\rho_0 \frac{\partial^2 \mathbf{u}(\mathbf{X},t)}{\partial t^2} = -\vec{\nabla}_{\mathrm{X}} \cdot \boldsymbol{\sigma}(\mathbf{u},T) + \mathbf{f}(\mathbf{X},t), \tag{1a}$$

with the boundary condition

$$\mathbf{u}(\mathbf{X},t) = \mathbf{g}(\mathbf{X},t), \quad \mathbf{X} \in \Gamma_d, \tag{1b}$$

$$\boldsymbol{\sigma} \cdot \vec{n} = \mathbf{t}(\mathbf{X},t), \quad \mathbf{X} \in \Gamma_n, \tag{1c}$$

and the initial condition

$$\mathbf{u}(\mathbf{X},t=0) = \mathbf{u}_0(\mathbf{X}), \quad \mathbf{X} \in \mathcal{D}_0, \tag{1d}$$

$$\frac{\partial \mathbf{u}}{\partial t}(\mathbf{X},t=0) = \mathbf{v}_0(\mathbf{X}), \quad \mathbf{X} \in \mathcal{D}_0. \tag{1e}$$

$\mathbf{X}$ is the independent variable for the position vectors of the material particles in the reference configuration, t is the independent variable for time. $\vec{n}$ is the outward unit normal vector on the boundary. We adopt the Lagrangian description in Eq. (1). $\mathbf{u}(\mathbf{X}, t)$ is the displacement, $\mathbf{f}$ is the body force, $\mathbf{g}(\mathbf{X}, t)$ is the prescribed displacement on boundary Γ_d, and $\mathbf{t}(\mathbf{X}, t)$ is the prescribed traction on boundary Γ_n. We assume Γ_d and Γ_n are non-overlapping and their union covers the entire boundary $\partial\mathcal{D}_0$. $\mathbf{u}_0(\mathbf{X})$ is the initial displacement, which on boundary Γ_d should be equal to $\mathbf{g}(\mathbf{X}, t)$ at time zero. $\mathbf{v}_0(\mathbf{X})$ is the initial velocity. We apply *small strain theory* for relating the stress and displacement where the displacement is assumed to be much smaller than any relevant dimension of the body, so that its geometry and the constitutive properties of the material (such as density and stiffness) at each point of space can be assumed to be unchanged by the deformation. The nominal stress tensor $\boldsymbol{\sigma}$ is directly related with the symmetric strain tensor $\boldsymbol{\epsilon}$ and the thermal expansion for isotropic materials

$$\boldsymbol{\sigma} = \lambda \,\mathrm{tr}(\boldsymbol{\epsilon})\mathbf{I} + 2\mu\boldsymbol{\epsilon} - (3\lambda + 2\mu)\alpha(T - T_0)\mathbf{I}, \tag{1f}$$

where λ and μ are *Lamé constants* and can be evaluated from Young's modulus E and Poisson's ratio η,

$$\lambda = \frac{\nu E}{(1+\eta)(1-2\eta)}, \tag{1g}$$

$$\mu = \frac{E}{2(1+\eta)}, \tag{1h}$$

and α is the thermal expansion coefficient. The subscript X is used to denote that the divergence operation is defined on the reference domain. Subscript x will appear later for denoting the operations on the deformed domain. T is the temperature and T_0 is the strain free temperature or reference temperature. $\mathrm{tr}(\cdot)$ represents a trace operation on a tensor and $\mathbf{I}$ is the identity tensor. The strain tensor is evaluated from the displacement with the strain-displacement equations

$$\boldsymbol{\epsilon} = \frac{1}{2}\left(\vec{\nabla}_{\mathrm{X}}\mathbf{u} + \vec{\nabla}_{\mathrm{X}}^{T}\mathbf{u}\right). \tag{1i}$$

ρ_0 is the original density without displacement at the reference temperature.

The thermal conduction equation for temperature is defined on the deformed domain $\mathcal{D}$

$$\rho c_p \frac{\partial T(\mathbf{x}, t)}{\partial t} = -\vec{\nabla}_{\mathrm{x}} \cdot k\vec{\nabla}_{\mathrm{x}} T + \mathbb{P}(\mathbf{x}, t), \tag{2a}$$

$$\mathbb{P}(\mathbf{x}, t) \equiv \sum_{g=1}^{G} \frac{\rho}{\rho_0} \kappa\Sigma_{f,g}\Phi_g(\mathbf{x}, t), \tag{2b}$$

where $\mathbb{P}$ is the energy deposition from neutron reactions, $\kappa\Sigma_{f,g}$ is the energy deposition cross sections and G is the number of energy groups. These cross sections are proportional to the current mass density. We assume all energy is from neutron induced fission and deposited locally. c_p is the heat capacity; k is the thermal conductivity. We apply the heat flux boundary condition

$$k\vec{\nabla}_{\mathrm{x}} T(\mathbf{x}, t) \cdot \vec{n} = h_b(T - T_0), \mathbf{x} \in \partial\mathcal{D} \tag{2c}$$

and set the initial temperature to be uniform

$$T(\mathbf{x}, t = 0) = T_0, \mathbf{x} \in \mathcal{D}. \tag{2d}$$

We assume that the mechanical energy is small compared with the total heat generated by neutron reaction so its contribution to heat conduction can be neglected. ρ is the time-dependent current density on the deformed domain,

$$\rho(t) = \frac{\rho_0}{\det(\vec{\nabla}_{\mathrm{X}}\mathbf{u}(t) + \mathbf{I})}, \tag{3}$$

where $\det(\cdot)$ is the determinant of a tensor.

The multigroup neutron transport equation is also defined on the deformed domain $\mathcal{D}$ with the two-dimensional unit sphere $\mathcal{S}$ as the angular domain,

$$\begin{aligned}\frac{\partial}{\partial t}\left(\frac{\Psi_g}{v_g}\right) = {} & \vec{\Omega} \cdot \vec{\nabla}_{\mathrm{x}}\Psi_g + \frac{\rho}{\rho_0}\Sigma_{t,g}\Psi_g(\mathbf{x}, \vec{\Omega}, t) \\ & - \sum_{g'=1}^{G} \int_{\mathcal{S}} \frac{\rho}{\rho_0}\Sigma_{s,g'\to g}(\vec{\Omega} \cdot \vec{\Omega}')\Psi_g(\vec{\Omega}')d\Omega' \\ & - \delta\frac{\chi_{g,p}}{4\pi}(1 - \sum_{i=1}^{I}\beta_i)\mathbb{f} - \frac{\chi_{g,i}}{4\pi}\sum_{i=1}^{I}\lambda_i C_i, \quad g = 1, \cdots, G \end{aligned} \tag{4a}$$

$$\Phi_g(\mathbf{x}) \equiv \int_{\mathcal{S}} \Psi_g d\Omega, \quad g = 1, \cdots, G \tag{4b}$$

$$\mathbb{f}(\mathbf{x}, t) \equiv \sum_{g'=1}^{G} \frac{\rho}{\rho_0}\nu\Sigma_{f,g'}\Phi_g \tag{4c}$$

$$\frac{\partial C_i}{\partial t} = \beta_i\mathbb{f} - \lambda_i C_i(\mathbf{x}, t), \quad i = 1, \cdots, I, \tag{4d}$$

with vacuum boundary condition

$$\Psi_g(\mathbf{x}, \vec{\Omega}, t) = 0, \mathbf{x} \in \mathcal{D}, \text{and } \vec{\Omega} \cdot \vec{n} < 0. \tag{4e}$$

$\vec{\Omega}$ is the independent angular variable for neutron direction of motion, Ψ_g is the g-th group angular flux, C_i is the concentration of the i-th delayed neutron precursor (DNP), Φ_g is the g-th group scalar flux, $\mathbb{f}$ is the fission-neutron production rate. $\Sigma_{t,g}$, $\Sigma_{s,g'\to g}$ and $\Sigma_{f,g'}$ are the total, differential scattering and fission cross sections respectively, that are affected by the local density change by the factor $\frac{\rho}{\rho_0}$. v_g is the averaged neutron velocity of g-th group, ν is the averaged number of neutrons emitted per fission. $\chi_{g,p}$ is the prompt fission spectrum, while $\chi_{g,i}$ is the spectrum of the i-th DNP. λ_i is the decay constant of the i-th DNP, β_i is the fraction of the i-th delayed neutrons of all fission induced neutrons. We assume that the body movement speed $\partial\mathbf{u}/\partial t$ is negligibly small with respect to the neutron velocities, so we can define the neutron transport equation simply on the displaced field. The Doppler feedback effect can be neglected and the macroscopic cross sections are assumed constant, i.e. spectrum for generating these cross sections are fixed, during the transient. We also neglect the thermal expansion effect on the DNP concentrations in Eq. (4d). The initial condition of the multigroup neutron transport equation

is obtained by solving a k-eigenvalue problem on the reference domain $\mathcal{D}_0$,

$$\vec{\Omega}\cdot\vec{\nabla}_{\mathrm{X}}\Psi_g+\Sigma_{t,g}\Psi_g=\sum_{g'=1}^{G}\int_S\Sigma_{s,g'\to g}(\vec{\Omega}\cdot\vec{\Omega}')\Psi_g(\vec{\Omega}')d\Omega'+\frac{1}{k}\frac{\chi_g}{4\pi}\mathbb{f},\quad g=1,\cdots,G; \tag{4f}$$

$$\chi_g\equiv\chi_{g,p}(1-\sum_{i=1}^{I}\beta_i)+\sum_{i=1}^{I}\chi_{g,i}\beta_i, \tag{4g}$$

$$C_i(\vec{r},t=0)=\frac{\beta_i\mathbb{f}}{k\lambda_i},\quad i=1,\cdots,I, \tag{4h}$$

where all cross sections are evaluated at the beginning of the transient. k is the fundamental eigenvalue. The flux is normalized such that the power is equal to a certain value denoted by P_0. We can find the adjoint solution Ψ_g^* of this k-eigenvalue problem, which will be used for evaluating the total effective DNP fraction:

$$\beta_{\mathrm{eff}}\equiv\frac{\left(\sum_{i=1}^{I}\beta_i\sum_{g=1}^{G}\chi_{g,i}\Phi_g^*,\sum_{g'=1}^{G}\nu\Sigma_{f,g'}\Phi_{g'}\right)_{\mathcal{D}_0}}{\left(\sum_{g=1}^{G}\chi_g\Phi_g^*,\sum_{g'=1}^{G}\nu\Sigma_{f,g'}\Phi_{g'}\right)_{\mathcal{D}_0}}, \tag{4i}$$

as a measure of the reactivity insertion. The transient is initiated by a given reactivity insertion with δ as

$$\delta=\gamma\frac{\beta_{\mathrm{eff}}}{k}. \tag{5}$$

The Godiva benchmark can be modeled using 1D spherical coordinates with radii ranging from 0 to R. The initial outer radius R_0 together with some other input parameters are listed in Table I. The body force $\mathbf{f}$, displacement of the center of the sphere $\mathbf{u}(r=0,t)$, traction at the outer sphere $\mathbf{t}(R_0,t)$ and the initial displacement $\mathbf{u}_0(r)$ are all set to zero. The leakage of heat from the sphere is small, so we assume it to be zero by setting $h_b=0$. It is noted that changing the reference temperature does not affect the calculation. Multigroup cross sections were generated with Serpent [13] with 93.5% U-235 enrichment at the reference state with a temperature 293.6K. The energy group boundary with eight groups in Table II are adapted from COMBINE [14]. DNP data, including the fraction, decay constant, are generated with Meulekamp's method. All delayed groups have the same delayed neutron spectrum.

TABLE I: Inputs.

Name	Value	Unit
Radius (R_0)	8.7407	cm
Young's modulus (E)	2.08×10^{12}	g/cm/s^2
Poisson's ratio (η)	0.23	unitless
Thermal expansion coefficient (α)	1.39×10^{-5}	1/K
Initial density (ρ_0)	18.74	g/cm^3
Heat capacity (c_p)	0.1177	J/g/K
Thermal conductivity (k)	0.275	W/cm/K
Reference temperature (T_0)	293.6	K
Reactivity insertion γ	1.05	\$
Initial total power P_0	1	W

TABLE II: Energy boundary for Serpent tallies.

Group index g	Upper bound	Lower bound
1	16.9MeV	2.87MeV
2	2.87MeV	1.35MeV
3	1.35MeV	0.821MeV
4	0.821MeV	0.388MeV
5	0.388MeV	0.111MeV
6	0.111MeV	15.0keV
7	15.0keV	3.36keV
8	3.36keV	0.001eV

The obtained eigenvalue is $0.994912\pm5.1pcm$. Because the cross sections are homogenized over the entire sphere, it is expected that the eigenvalue k from Rattlesnake, the transport solver called by MAMMOTH, will be slightly different from this reference value. Multigroup macroscopic cross sections and DNP data are provided in Table III and Table IV.

III. METHODS

The weak form for Eq. (1) with a homogeneous boundary condition and zero external load is

$$b_s(\mathbf{u}^*,\mathbf{u})=(\mathbf{u}^*,\rho_0\ddot{\mathbf{u}})_{\mathcal{D}_0}+(\nabla_{\mathbf{X}}\mathbf{u}^*,\boldsymbol{\sigma})_{\mathcal{D}_0}=0. \tag{6}$$

We did not apply the Rayleigh damping in this calculation. The weak form for Eq. (2) with zero heat flux on the boundary is

$$b_t(T^*,T)=\left(T^*,\rho c_p\dot{T}\right)_{\mathcal{D}}+(\nabla_{\mathbf{x}}T^*,k\nabla_{\mathbf{x}}T)_{\mathcal{D}}-(T^*,\mathbb{P})_{\mathcal{D}}=0. \tag{7}$$

We use the continuous finite element method (CFEM) for discretizing the weak forms Eq. (6) and Eq. (7). Superscript $*$ is used to denote the test functions. These forms can be transferred to spherical coordinates straightforwardly by applying the differential element $4\pi r^2$ in the definition of the inner product $(\cdot,\cdot)$. We are going to use SAAF-SN (self-adjoint angular flux, discrete ordinates) with CFEM for discretizing the multigroup transport equation. The weak form for the multigroup transport equation in 1D spherical coordinate is more involved due to the streaming. Because the weak form, to the best of the authors' knowledge, has not been reported in literature, we derive it in the first subsection of this section. It is noted that the derivation applies to general curvilinear coordinates. The time integration scheme for solid-mechanics will also briefly discussed in the second subsection. We solve the equations with the Lagrangian mesh, i.e. we set up two meshes, one is the reference mesh, another is the displaced mesh modified from the reference mesh with the current displacement $\mathbf{u}$. Element quadrature points remain coincident with material points in this way. Thus, variables or their time derivatives evaluated on the coincident quadrature points of the reference and the displaced mesh are the same. Contribution of terms to the residual and Jacobian are assembled into the system with the selection of one of the two meshes. We use the PJFNK solver to solve the coupled system with the block-diagonal matrix except the off-diagonal matrices for angular fluxes from the

TABLE III: Multigroup macroscopic cross sections.

Type \ g		1	2	3	4	5	6	7	8
$\Sigma_{t,g}$ (1/cm)		0.367450	0.342842	0.326579	0.379136	0.486052	0.608836	0.757914	0.959055
$\nu\Sigma_{f,g}$ (1/cm)		0.164414	0.153788	0.135015	0.127025	0.144942	0.189544	0.322009	0.638574
$\kappa\Sigma_{f,g}$ (J/cm)		1.78775E-12	1.87762E-12	1.71939E-12	1.65049E-12	1.90041E-12	2.52369E-12	4.28227E-12	8.48906E-12
$\chi_{g,p}$		2.38740E-01	3.53431E-01	1.75297E-01	1.46300E-01	7.22222E-02	1.33037E-02	6.31710E-04	7.46555E-05
v_g (cm/s)		2.78673E+09	1.91548E+09	1.41405E+09	1.04132E+09	6.61301E+08	3.43040E+08	1.33985E+08	5.41897E+07
$\chi_{g,1\text{-}6}$		3.49934E-04	4.36339E-02	1.36892E-01	3.50812E-01	3.49868E-01	1.06490E-01	9.98797E-03	1.96588E-03
	g'								
$\Sigma_{s,0,g\to g'}$ (1/cm)	1	2.22648E-01							
	2	1.95370E-02	1.99476E-01						
	3	2.10732E-02	2.42596E-02	2.06087E-01					
	4	2.94706E-02	3.33968E-02	3.59861E-02	2.87050E-01				
	5	1.81941E-02	2.11189E-02	2.19285E-02	3.03808E-02	4.03632E-01			
	6	3.11190E-03	3.47807E-03	4.15951E-03	3.45022E-03	1.10754E-02	5.05712E-01		
	7	1.36708E-04	1.52122E-04	1.77450E-04	1.08876E-04	1.83546E-04	1.04971E-03	5.75747E-01	
	8	2.42681E-05	2.75950E-05	3.17398E-05	1.89209E-05	1.19789E-05	4.92712E-05	5.96135E-04	5.74718E-01
$\Sigma_{s,1,g\to g'}$ (1/cm)	1	1.66664E-01							
	2	8.29032E-04	1.12303E-01						
	3	2.69536E-04	4.13057E-04	9.26913E-02					
	4	2.25935E-04	1.85691E-04	5.02009E-04	1.02220E-01				
	5	4.09453E-05	2.04983E-05	4.82467E-05	5.78684E-05	8.71538E-02			
	6	-4.01827E-06	-1.80321E-06	-3.24884E-06	-8.06327E-06	-2.14750E-04	4.48213E-02		
	7	-1.27406E-07	-5.57798E-08	-7.12065E-07	-6.41959E-07	1.29444E-06	-8.38584E-05	9.37723E-03	
	8	2.35053E-06	1.58656E-06	1.83790E-06	5.45410E-07	-3.08191E-07	-8.85951E-08	-2.06829E-04	2.76586E-03
$\Sigma_{s,2,g\to g'}$ (1/cm)	1	1.33702E-01							
	2	9.67644E-05	7.99193E-02						
	3	9.47327E-05	-1.10916E-04	4.91432E-02					
	4	1.56181E-04	1.03313E-04	-2.52529E-04	3.77909E-02				
	5	8.39613E-05	6.21568E-05	9.99613E-05	-1.91458E-04	1.81973E-02			
	6	1.30830E-05	1.23796E-05	1.68551E-05	1.93257E-05	-9.20864E-05	3.39616E-03		
	7	7.93967E-07	2.49931E-07	6.24739E-07	5.08715E-07	2.61141E-08	-2.38672E-06	1.10208E-04	
	8	2.08141E-07	3.21020E-07	3.56209E-07	1.20735E-07	4.46787E-08	-8.04760E-08	1.81423E-07	2.12044E-04
$\Sigma_{s,3,g\to g'}$ (1/cm)	1	1.07243E-01							
	2	7.31226E-05	6.30333E-02						
	3	2.30256E-05	5.84943E-05	3.33670E-02					
	4	1.01128E-05	2.48752E-05	-3.37336E-05	1.43273E-02				
	5	3.67997E-06	1.04181E-05	6.98853E-07	-8.01657E-05	2.84272E-03			
	6	2.21223E-07	9.62818E-07	1.75419E-06	-1.82636E-06	-1.28080E-05	6.78219E-05		
	7	4.94397E-07	-2.14445E-07	-3.07215E-07	9.92446E-09	-3.21352E-07	-1.75764E-07	-4.48921E-05	
	8	1.25894E-07	5.71855E-08	-4.84467E-08	2.71818E-08	4.50893E-08	2.71803E-07	6.88755E-06	9.35099E-04
$\Sigma_{s,4,g\to g'}$ (1/cm)	1	8.51221E-02							
	2	1.19693E-04	4.38491E-02						
	3	-2.09279E-05	-1.61544E-05	1.36964E-02					
	4	-1.22633E-05	-1.06642E-05	-4.03557E-05	3.32472E-03				
	5	-3.55973E-06	4.29501E-07	3.24775E-06	-8.50891E-06	2.21346E-04			
	6	-2.99110E-07	-7.70798E-07	-7.38745E-07	3.44704E-08	-1.22655E-06	-2.59621E-04		
	7	-3.54124E-07	-1.10112E-08	-3.87219E-07	6.67530E-08	-1.97758E-07	1.17313E-06	-5.09103E-05	
	8	-2.96991E-08	7.35283E-08	8.79001E-09	-5.45025E-08	8.85128E-09	3.29318E-08	-3.66186E-06	1.17183E-03

TABLE IV: DNP data.

Type	1	2	3	4	5	6
β_i	0.000243519	0.00121692	0.00117171	0.00261101	0.00110058	0.000462663
λ_i (1/s)	0.0133394	0.0327156	0.120832	0.303363	0.851952	2.86128

streaming term on the curvilinear coordinate being the preconditioning matrix. The row and column block index of the matrix correspond to the primal variables. The preconditioning system is solved with SuperLU_DIST [15].

1. Weak form for the transport equation in curvilinear coordinates

The derivation of weak forms for the curvilinear coordinates relies on the observation of the differences of the following three operators: the streaming operator $\partial_{\vec{\Omega}}\Psi$, the operator with divergence $\vec{\nabla}\cdot(\vec{\Omega}\Psi)$ and the operator with gradient $\vec{\Omega}\cdot\vec{\nabla}\Psi$. In Cartesian coordinates, all of them are identical, which explains why $\vec{\Omega}\cdot\vec{\nabla}\Psi$ is typically used to denote the streaming operator. We introduce this new notation $\partial_{\vec{\Omega}}\Psi$ to emphasize the partial derivative of the angular flux along the streaming direction. We define two new operators for the difference of these operators:

$$E[\Psi] \equiv \partial_{\vec{\Omega}}\Psi - \vec{\nabla}\cdot(\vec{\Omega}\Psi), \tag{8}$$

$$E_2[\Psi] \equiv \vec{\nabla}\cdot(\vec{\Omega}\Psi) - \vec{\Omega}\cdot\vec{\nabla}\Psi, \tag{9}$$

and summarize them in Table V. It is noted that E_2 does not include the angular derivatives. In spherical coordinates (r,θ,ϕ) in space, which are the symbols for the radial, zenith and azimuth angle coordinates, the angular polar angle $\varphi \in [0,\pi]$ is with respect to the unit vector $\hat{e}_r$. We typically use the cosine of the polar angle $\mu = \cos\varphi$ as the polar variable. And the azimuthal angle ω is measured in the plane of $\hat{e}_\theta, \hat{e}_\phi$ unit vectors starting from $\hat{e}_\theta$. In cylindrical coordinates (r,ϕ,z) in space, which are the symbols for the radial, azimuth angle and z coordinates, the angular polar angle $\varphi \in [0,\pi]$ is with respect to the unit vector $\hat{e}_z$. $\mu = \cos\varphi$ and the azimuthal angle ω is measured in the plane of $\hat{e}_r, \hat{e}_\phi$ unit vectors starting from $\hat{e}_r$. In 1D R-spherical coordinate, the ω-derivative in E and the term in E_2 involving $\cos\omega$ are zero. The derivation of the weak form uses the divergence theorem along with integration by parts:

TABLE V: Streaming operator in curvilinear coordinates.

Coordinate type	$E[\Psi]$	$E_2[\Psi]$
Cartesian	0	0
Spherical	$\frac{1}{r}\frac{\partial}{\partial\mu}\left[(1-\mu^2)\Psi\right] - \frac{\cos\theta}{r\sin\theta}\frac{\partial}{\partial\omega}(\Psi\sqrt{1-\mu^2}\sin\omega)$	$\left(\frac{2\mu}{r} + \sqrt{1-\mu^2}\cos\omega\frac{\cos\theta}{r\sin\theta}\right)\Psi$
Cylindrical	$-\frac{1}{r}\frac{\partial}{\partial\omega}(\Psi\sqrt{1-\mu^2}\sin\omega)$	$\frac{\sqrt{1-\mu^2}\cos\omega}{r}\Psi$

$$\left(\Psi^*, \partial_{\vec{\Omega}}\Psi\right)_{\mathcal{D}} = \langle\Psi^*,\Psi\rangle_{\partial\mathcal{D}} - \left(\vec{\Omega}\cdot\vec{\nabla}\Psi^*,\Psi\right)_{\mathcal{D}} + (\Psi^*, E[\Psi])_{\mathcal{D}}, \tag{10}$$

where

$$(a,b)_{\mathcal{D}} \equiv \int_{\mathcal{D}} a(\mathbf{x})b(\mathbf{x})v\,dx, \tag{11}$$

$$\langle a,b\rangle_{\partial\mathcal{D}} \equiv \int_{\partial\mathcal{D}} a(\mathbf{x})b(\mathbf{x})v\vec{\Omega}\cdot\vec{n}\,ds. \tag{12}$$

a and b are two generic functions defined over the solution domain $\mathcal{D}$ or the boundary $\partial\mathcal{D}$. v is the differential element applied to curvilinear coordinates. It is one for Cartesian coordinate, $4\pi r^2$ for 1D R-spherical coordinate.

We will derive the SAAF weak form for curvilinear coordinates. To simplify the notation, we consider the mono-energetic steady-state transport equation with an isotropic scattering source $\frac{1}{4\pi}\Sigma_s\int_{4\pi}\Psi\,d\Omega$, a fixed extraneous source Q and vacuum boundaries. We also do not include the void treatment. It is noted that all of these simplifications can be removed in the complete weak form without fundamental difficulty. Following the same derivation of SAAF weak form in [16], we end up with the following bilinear and linear forms:

$$b(\Psi^*,\Psi) \equiv \underline{\left(\frac{1}{\Sigma_t}\vec{\Omega}\cdot\vec{\nabla}\Psi^*, \vec{\Omega}\cdot\vec{\nabla}\Psi\right)} + (\psi^*, \Sigma_t\Psi) + \langle\Psi^*,\Psi\rangle^+ + \underline{\left(\frac{1}{\Sigma_t}\vec{\Omega}\cdot\vec{\nabla}\Psi^* + \Psi^*, E[\Psi]\right) + \left(\frac{1}{\Sigma_t}\vec{\Omega}\cdot\vec{\nabla}\Psi^*, E_2[\Psi]\right)} - \left(\frac{1}{\Sigma_t}\vec{\Omega}\cdot\vec{\nabla}\Psi^* + \Psi^*, \frac{1}{4\pi}\Sigma_s\int_{4\pi}\Psi\,d\Omega\right) \tag{13}$$

$$l(\Psi^*) \equiv \left(\frac{1}{\Sigma_t}\vec{\Omega}\cdot\vec{\nabla}\Psi^* + \Psi^*, Q\right). \tag{14}$$

The two underlined terms in addition to the Cartesian bilinear form are due to the streaming in curvilinear coordinate. Few notations used in the above forms are defined as

$$(a,b) \equiv \int_{\mathcal{D}}\int_{4\pi} a(\mathbf{x})b(\mathbf{x})v\,d\Omega\,dx, \tag{15}$$

$$\langle a,b\rangle^+ \equiv \int_{\partial\mathcal{D}}\int_{\vec{\Omega}\cdot\vec{n}>0} a(\mathbf{x})b(\mathbf{x})v\left|\vec{\Omega}\cdot\vec{n}\right|\,d\Omega\,ds, \tag{16}$$

$$\langle a,b\rangle^- \equiv \int_{\partial\mathcal{D}}\int_{\vec{\Omega}\cdot\vec{n}<0} a(\mathbf{x})b(\mathbf{x})v\left|\vec{\Omega}\cdot\vec{n}\right|\,d\Omega\,ds. \tag{17}$$

In 1D R-spherical coordinate, the extra terms can be spelled out as

$$\left(\frac{1}{\sigma_t}\mu\frac{\partial}{\partial r}\Psi^* + \Psi^*, \frac{1}{r}\frac{\partial}{\partial\mu}[(1-\mu^2)\Psi]\right) + \left(\frac{1}{\sigma_t}\mu\frac{\partial}{\partial r}\Psi^*, \frac{2}{r}\mu\Psi\right).$$

These terms can be discretized angularly with SN given an angular quadrature $\{\mu_m, w_m, m = 1,\cdots,M\}$ as

$$\sum_{m=1}^{M} w_m\left(\frac{1}{\sigma_t}\mu_m\frac{\partial}{\partial r}\Psi_m^* + \Psi_m^*, \frac{1}{r}\frac{\partial}{\partial\mu}[(1-\mu^2)\Psi]\Big|_{\mu=\mu_m}\right)_{\mathcal{D}} + \sum_{m=1}^{M} w_m\left(\frac{1}{\sigma_t}\mu_m\frac{\partial}{\partial r}\Psi_m^*, \frac{2}{r}\mu_m\Psi_m\right)_{\mathcal{D}}, \tag{18}$$

where $\Psi_m = \Psi(\mu_m)$. The μ-derivative can be evaluated with the following generic formulation:

$$\frac{\partial}{\partial\mu}[(1-\mu^2)\Psi]\Big|_{\mu-\mu_m} = \sum_{n=1}^{M}\beta_{m,n}\Psi_n. \tag{19}$$

We first follow the similar procedure in Ref. [17] to obtain these βs. We let

$$\frac{\partial}{\partial\mu}(1-\mu^2)\Psi\Big|_{\mu=\mu_m} = 2\frac{\alpha_{m+1/2}\Psi_{m+1/2} - \alpha_{m-1/2}\Psi_{m-1/2}}{w_m}, \tag{20}$$

and obtain the constraints,

$$\alpha_{M+1/2} = \alpha_{1/2} = 0, \tag{21}$$
$$\alpha_{m+1/2} = \alpha_{m-1/2} - w_m\mu_m, m = 1, \cdots, M. \tag{22}$$

We also include the same approximation

$$\Psi_{m+1/2} = 2\Psi_m - \Psi_{m-1/2}, m = 1, \cdots, M. \tag{23}$$

We need a dummy direction with $\mu = -1$ for $\psi_{1/2}$ indexed as $m = 0$ later to start solving the angular fluxes sequentially from $m = 1$ to M. Eq. (19) on this dummy direction is simply equal to 2ψ. We call this direction dummy because its angular flux does not contribute the evaluation of the angular flux moments. It is desired to add another dummy direction $\mu = 1$ denoted with $m = M + 1$ for the adjoint calculation. We propose the following equation

$$\Psi_{M+1} = 2\Psi_{M+1} - (2\Psi_M - \Psi_{M-1/2}). \tag{24}$$

to artificially bring in the coupling from the directions of $m = 0, \cdots, M$ for this additional dummy direction. Finally, we obtain

$$\beta_{m,n} = \begin{cases} (-1)^m \frac{2}{w_m}(\alpha_{m+1/2} + \alpha_{m-1/2}), & n = 0, 0 < m \le M; \\ (-1)^{n+m} \frac{4}{w_m}(\alpha_{m+1/2} + \alpha_{m-1/2}), & 0 < n < m, 0 < m \le M; \\ \frac{4}{w_m}\alpha_{m+1/2}, & n = m, 0 < m \le M; \\ -2\mu_0 & n = m = 0; \\ 0 & n > m; 0 \le m \le M \\ 2, & n = 0, m = M + 1; \\ (-1)^n 4, & 0 < n \le M; m = M + 1 \\ -4 & n = m = M + 1. \end{cases} . \tag{25}$$

We can prove

$$\sum_{n=0}^{m} \beta_{m,n} = -2\mu_m. \tag{26}$$

So Eq. (18) is indeed equal to zero when applying the P_0 projection, i.e. assuming angular fluxes and their tests are angular independent with $\Psi_m^* = \Phi^*, \Psi_m = \Phi$. The matrix formed by the βs is lower triangular. Because this scheme enables the sequential solving of angular fluxes once the source is known, we label it as the sweeping scheme. The mathematical adjoint, i.e. the transpose of the extra streaming terms, can be derived following the similar procedure in [18]. The solution from the mathematical adjoint equation is required for evaluating the β_{eff}.

We will also present another new way of evaluating the μ-derivative and show the superior angular convergence of this treatment with numerical results. From the discrete angular fluxes $\Psi_m, m = 1, \cdots, M$, we evaluate the angular flux moments up to order $M - 1$ with

$$\Phi_\ell = \sum_{m=1}^{M} w_m P_\ell(\mu_m)\Psi_m, \ell = 0, \cdots, M - 1, \tag{27}$$

where P_ℓ is the ℓ-th order of Legendre polynomial. Then we can construct the continuous angular flux

$$\Psi(\mu) = \sum_{\ell=0}^{M-1} \frac{2\ell + 1}{2} P_\ell(\mu) \sum_{m=1}^{M} w_m P_\ell(\mu_m)\Psi_m, \tag{28}$$

which allows us to evaluate $\frac{\partial}{\partial\mu}[(1-\mu^2)\Psi]\Big|_{\mu=\mu_m}$ as

$$\sum_{\ell=0}^{M-1} \frac{2\ell + 1}{2} \left((\ell - 1)\mu_m P_\ell(\mu_m) - (l + 1)P_{\ell+1}(\mu_m)\right) \sum_{n=1}^{M} w_n P_\ell(\mu_n)\Psi_n, \tag{29}$$

i.e.

$$\beta_{m,n} = \sum_{\ell=0}^{M-1} \frac{2\ell + 1}{2} \left((\ell - 1)\mu_m P_\ell(\mu_m) - (l + 1)P_{\ell+1}(\mu_m)\right) w_n P_\ell(\mu_n). \tag{30}$$

We can prove that the same property Eq. (26) holds for these βs. Because $\mu_m = -\mu_{M+1-m}, w_m = w_{M+1-m}, m = 1, \cdots, M/2$, we have

$$\beta_{M+1-m,M+1-n} = -\beta_{m,n}, \tag{31}$$

which appears to be an appealing feature for adjoint calculations. With this treatment, β matrix is no longer lower triangular, meaning that we do not have an angular sweep to invert the streaming-collision operator. However, this is not necessarily considered a disadvantage with the deployed PJFNK solver. Plus this scheme does not require dummy directions. This scheme can also be used for evaluating the ω-derivative, $\frac{\partial}{\partial\omega}(\Psi\sqrt{1-\mu^2}\sin\omega)$, with SN. Because this scheme involves the spherical harmonics (Legendre in 1D) expansion of the angular flux, we label it as the PN scheme for evaluating the angular derivatives.

2. Time integration for solid-mechanics

Because significant numerical dispersion can occur in the time integration (hyperbolic nature of the dynamics equation) for solid-mechanics, the Newmark time integration is employed. In Newmark time integration, the current acceleration and velocity are written in terms of the displacement, velocity and acceleration at the previous time step and the current displacement:

$$\ddot{\mathbf{u}} = \frac{\mathbf{u} - \mathbf{u}^{old}}{n_a \Delta t^2} - \frac{\dot{\mathbf{u}}^{old}}{n_a \Delta t} + \frac{n_a - \frac{1}{2}}{n_a}\ddot{\mathbf{u}}^{old}, \tag{32}$$
$$\dot{\mathbf{u}} = \dot{\mathbf{u}}^{old} + (1 - n_v)\Delta t\ddot{\mathbf{u}}^{old} + n_v\Delta t\ddot{\mathbf{u}}, \tag{33}$$

where n_a and n_v are the Newmark time integration parameters. The equation can be substituted into the bilinear form to obtain a linear system of equations from which $\mathbf{u}$ at the current time step can be evaluated. This formulation bypasses the time integration schemes applied in the other physics, i.e. thermal conduction and neutron transport.

The Hilber-Hughes-Taylor (HHT) time integration scheme is built upon Newmark time integration. A HHT parameter n_{HHT} greater than or equal to 0 and less than or equal to 1 is introduced to alter the bilinear and linear form into:

$$b(\mathbf{u}, \mathbf{u}^*) = (\rho\ddot{\mathbf{u}}, \mathbf{u}^*)_{\mathcal{D}} + \left((1 + n_{\text{HHT}})\boldsymbol{\sigma} - \boldsymbol{\sigma}^{old}, \nabla_{\mathbf{X}}\mathbf{u}^*\right)_{\mathcal{D}}. \tag{34}$$

There are a total of three parameters affecting the time integration (two for Newmark integration and one for the HHT scheme). n_a and n_v are typically required parameters, while n_{HHT} defaults to zero. Implementation details can be found at MOOSE Wiki page [19].

IV. NUMERICAL RESULTS

We first investigated the angular convergence of two schemes of evaluating μ-derivative with the initial eigenvalue problem. A mesh with 40 uniform elements was used. First order Lagrange shape functions in space were used throughout this study. The convergence of k-effective with respect to the SN order was plotted in Fig. 1a. k-effective obtained with S48 PN scheme was used as the reference. The number of directions in the angular quadrature is two times the SN order. It is clear that the PN scheme for evaluating the angular

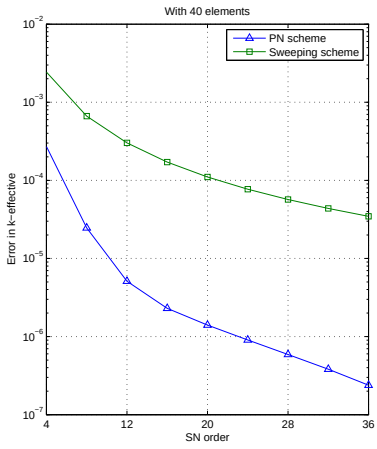

(a) Comparison between two μ-derivative schemes.

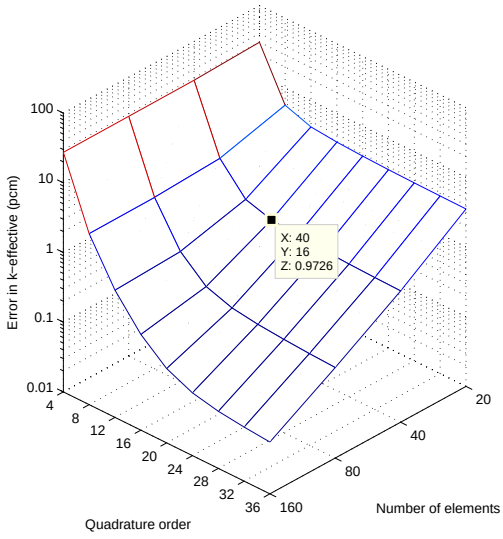

(b) Angular and spatial convergence.

Fig. 1: Convergence study with the initial eigenvalue problem.

derivatives with the same SN order gives a k-effective with much smaller error than the sweeping scheme. Thus, we used PN scheme in all our later calculations. We also did a quick convergence study on the mesh size and SN order with the initial eigenvalue problem. The results are shown in Fig. 1b. The reference solution was obtained with S48 and 640 uniform elements. Because 40 elements with S16 can already make the error in k-effective less than 1pcm, we used this combination in our transient calculations. The initial k-effective is 0.99571, 80 pcm different from the k-effective from Serpent. The evaluated beta effective is 688.0, 7.4pcm different from the Serpent value 680.6. The initial flux distribution along the radial direction is plotted in Fig. 2. The fluxes of the most

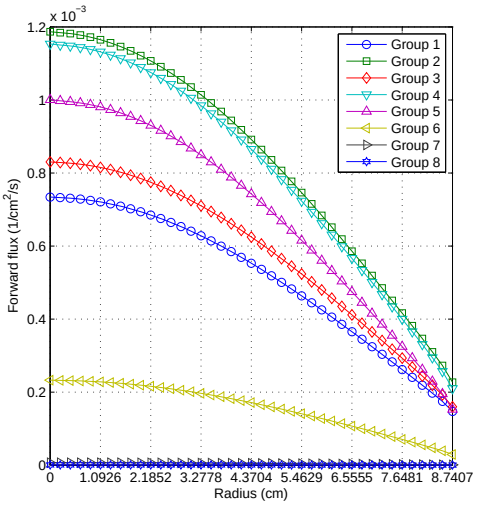

(a) Forward scalar fluxes.

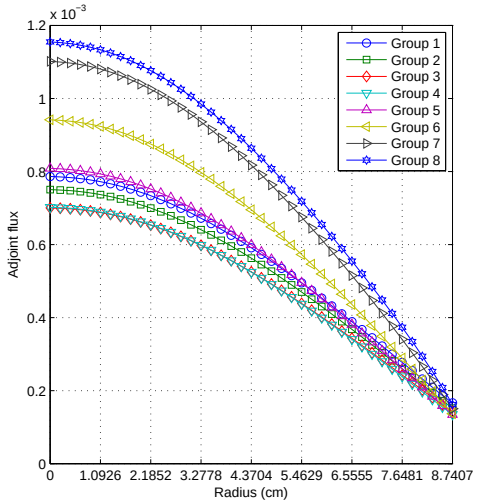

(b) Adjoint scalar fluxes.

Fig. 2: Initial fluxes.

thermal groups are fairly low in magnitude but the highest in importance.

The Newmark parameters were set as $n_a = 0.25$ and $n_v = 0.5$. In this particular calculation, we applied the HHT parameter n_{HHT} to 0. A backward Euler scheme was applied to thermal conduction and neutron transport. The time step size was chosen to be 1×10^{-7} seconds. The end time was set to 0.001 seconds. The total number of time steps was 10,000.

The total run time was 2.9hr using 8 cores of a 2.7 GHz 12-Core Intel Xeon E5 CPU. On average, each time step took about 1.05 seconds. Several quantities of interest (QoI), listed in Table VI, were plotted with time in Fig. 3, Fig. 4, Fig. 5 and Fig. 6. The peak power is 2.729GW at 0.3272ms.

TABLE VI: Transient quantities of interest.

Name	Unit	Equation
Total power	W	$\int_0^R \mathbb{P}(r,t) 4\pi r^2 \, dr$
Neutron leakage ratio	unitless	$\frac{4\pi R^2 \sum_{\mu_m>0} w_m \mu_m \Psi_{g,m}(r=R,t)}{\int_0^R \mathbb{f}(r,t) 4\pi r^2 \, dr}$
Outer displacement	cm	$\mathbf{u}(r=R,t)$
Outer velocity	cm/s	$\frac{\partial \mathbf{u}(r,t)}{\partial t}\Big\vert_{r=R}$
Outer acceleration	cm/s^2	$\frac{\partial^2 \mathbf{u}(r,t)}{\partial t^2}\Big\vert_{r=R}$
Average stress	g/cm/s^2	$\frac{\int_0^R \sigma(r,t) 4\pi r^2 \, dr}{\frac{4}{3}\pi R^3}$
Elastic energy ratio	unitless	$\frac{\int_0^R \frac{1}{2}\sigma(r,t)\epsilon(r,t) 4\pi r^2 \, dr}{\int_0^t \int_0^R \mathbb{P}(r,t') 4\pi r^2 \, dr \, dt'}$
Average temperature	K	$\frac{\int_0^R T(r,t) 4\pi r^2 \, dr}{\frac{4}{3}\pi R^3}$

The neutron leakage ratio does not change much with respect to its absolute value. The displacement is relatively small compared with the radius of the sphere. The ratio between elastic energy and the total thermal energy is relatively small, less than 1.4×10^{-4}. All of these results justify the initial approximations made in the model. Averaged temperature at 0.5 millisecond is 319.0K. The quickly accumulated thermal power causes the sphere to expand and eventually vibrate at a frequency of about 16 kHz around a radius extended by 0.003 centimeters higher from the initial radius 8.7407cm. The power reaches its first peak then drops due to loss of criticality caused by the thermal expansion. The trailing power around 1 MW is caused by the delayed neutrons.

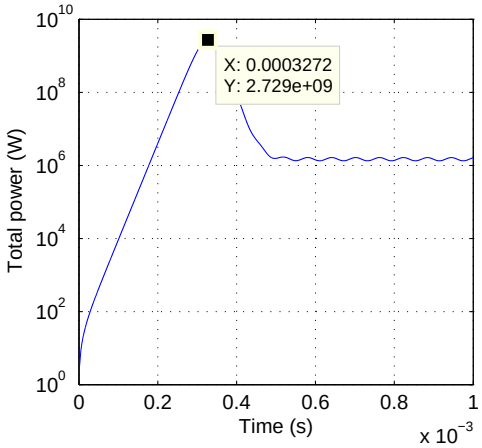

(a) Total power.

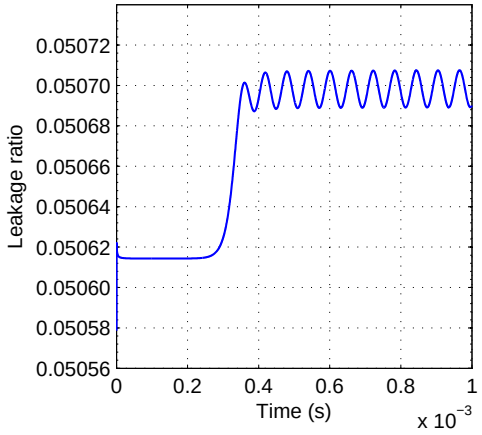

(b) Leakage ratio.

Fig. 3: Neutronics QoI versus time.

V. CONCLUSIONS

This paper details the Godiva benchmark problem for coupled neutronics and thermo-mechanics simulations. The weak form for the curvilinear coordinates including 1D R-spherical coordinate is derived. A PN scheme is proposed for evaluating the μ-derivative and numerical results are presented to show its superior convergence over the classic sweeping scheme. We solved this benchmark problem with MAMMOTH in a strongly coupled manner. Results of several quantities of interest during the transient are presented. It will be interesting to investigate the impact of a large initial reactivity insertion, where the small strain theory assumed in this paper may be invalid. Results up to seconds could be added in the future. We also expect the CPU time to be reduced substantially with the improved quasi-static (IQS) method.

VI. ACKNOWLEDGMENTS

This work is supported by the U.S. Department of Energy, under DOE Idaho Operations Office Contract DE-AC07-05ID14517. Accordingly, the U.S. Government retains a nonexclusive, royalty-free license to publish or reproduce the published form of this contribution, or allow others to do so, for U.S. Government purposes. The authors also thank the developers of MOOSE tensor mechanics module including Benjamin Spencer, Daniel Schwen for their code implementation and helpful discussions. The authors also thank Jean Ragusa at Texas A&M University for bringing our attention to the Godiva benchmark problem and helpful discussions.

REFERENCES

1. D. GASTON, C. NEWMAN, G. HANSEN, and D. LEBRUN-GRANDIE, "MOOSE: A parallel computational framework for coupled systems of nonlinear equations," *Nuclear Engineering and Design*, **239**, *10*, 1768–1778 (2009).
2. Y. WANG, S. SCHUNERT, B. A. BAKER, V. M. LABOURE, F. G. GLEICHER, J. ORTENSI, M. D. DEHART, and R. C. MARTINEAU, *Rattlesnake User Manual*, INL (2016).
3. R. WILLIAMSON, J. HALES, S. NOVASCONE, M. TONKS, D. GASTON, C. PERMANN, D. ANDRS,

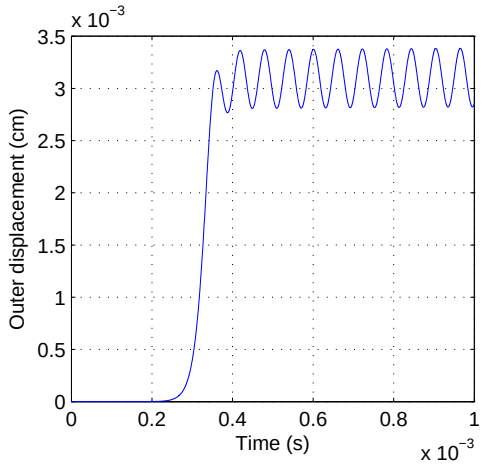

(a) Outer displacement.

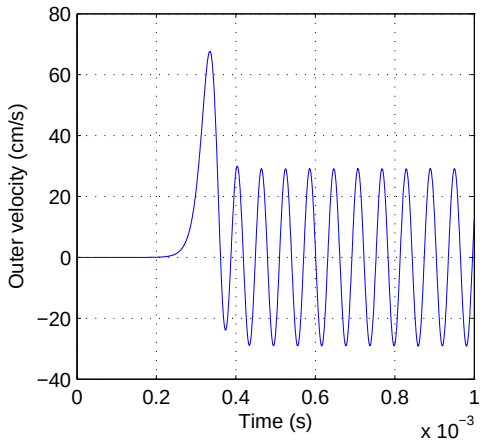

(b) Outer velocity.

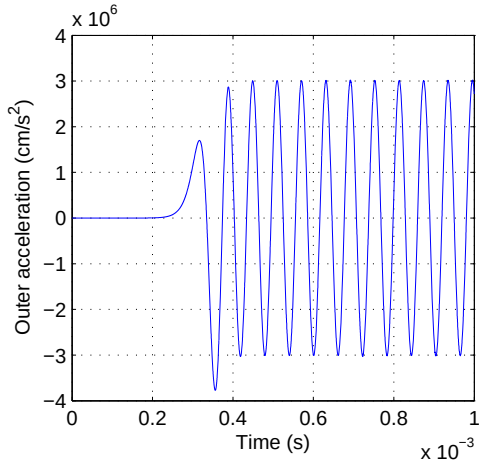

(c) Outer acceleration.

Fig. 4: Mechanics QoI versus time.

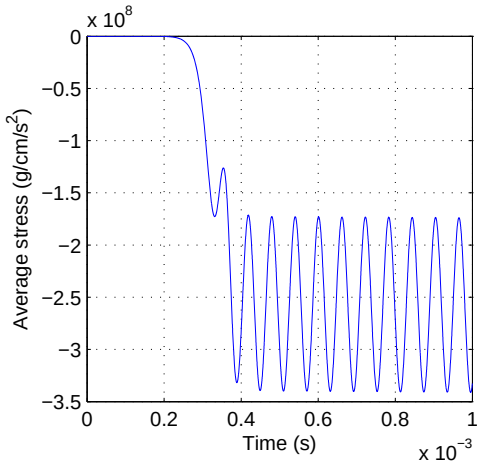

(a) Average stress.

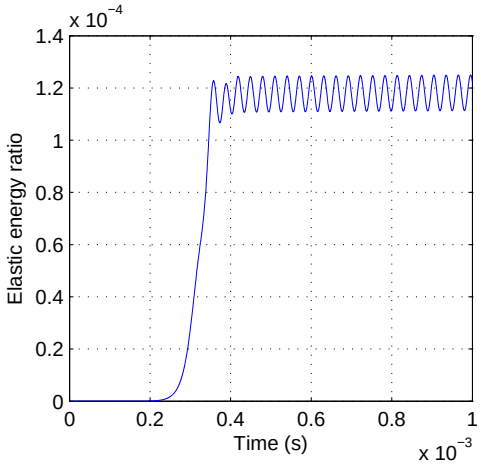

(b) Elastic energy ratio.

Fig. 5: Mechanics QoI versus time (continued).

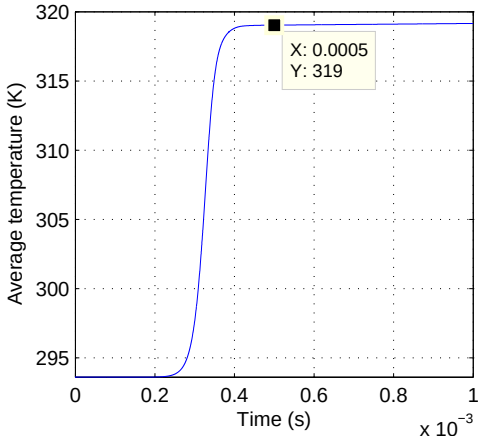

(a) Leakage ratio.

Fig. 6: Thermal QoI versus time.

and R. MARTINEAU, "Multidimensional multiphysics simulation of nuclear fuel behavior," *Journal of Nuclear Materials*, **423**, 149–163 (2012).

4. R. A. BERRY, J. W. PETERSON, H. ZHANG, R. C. MARTINEAU, H. ZHAO, L. ZOU, and D. ANDRS, "RELAP-7 Theory Manual," Research Report INL/EXT-14-31366, Idaho National Laboratory, Idaho Falls, ID

(December 2014).

5. J. HALES, M. TONKS, F. GLEICHER, B. SPENCER, S. NOVASCONE, R. WILLIAMSON, G. PASTORE, and D. PEREZ, "Advanced multiphysics coupling for LWR fuel performance analysis," *Annals of Nuclear Energy*, **84**, *1*, 98–110 (2015).
6. D. GASTON and ET AL., "Physics-based multiscale coupling for full core nuclear reactor simulation," *Annals of Nuclear Energy*, **84**, *1*, 45–54 (2015).
7. F. GLEICHER, J. ORTENSI, B. SPENCER, Y. WANG, S. NOVASCONE, J. HALES, D. GASTON, R. WILLIAMSON, and R. MARTINEAU, "The Coupling of the Neutron Transport Application Rattlesnake to the Nuclear Fuels Application BISON under the MOOSE Framework," in "PHYSOR 2014 - The Role of Reactor Physics Towards a Sustainable Future," The Westin Miyako, Kyoto, Japan (September 28 - October 3, 2014 2014).
8. F. GLEICHER, J. ORTENSI, Y. WANG, S. SCHUNERT, S. NOVASCONE, J. HALES, R. WILLIAMSON, A. SLAUGHTER, C. PERMANN, D. ANDRS, and R. MARTINEAU, "The Application of MAMMOTH for a Detailed Tightly Coupled Fuel Pin Simulation with a Station Blackout," in "Top Fuel 2016 - LWR Fuels with Enhanced Safety Performance," Boise, ID, USA (Sept. 11 - 16 2016).
9. R. PETERSON and G. NEWBY, "Lady Godiva - An unreflected U-235 Critical Assembly," Tech. Rep. LA-1614, Los Alamos National Laboratory (1953).
10. L. ENGLE, G. GRAVES, J. G.R. KEEPIN, J. ORNDOFF, and T. WIMETT, "Time Behavior of Godiva through Prompt Critical," Tech. Rep. LA-2029, Los Alamos National Laboratory (1956).
11. C. FIORINA, S. PELLONI, M. AUFIERO, and K. MIKITYUK, "A Time-Dependent Solver for Coupled Neutron-Transport Thermal-Mechanics Calculations and Simulation of a Godiva Prompt-Critical Burst," in "The 2014 22nd International Conference on Nuclear Engineering, ICONE22," Prague, Czech Republic (July 7–11 2014).
12. C. PATRICOT, A.-M. BAUDRON, and O. FANDEUR, "Interests of the Improved Quasi-Static Method for Multi-Physics Calculations Illustrated on a Neutronics-Thermomechanics Coupling," in "PHYSOR 2014 - The Role of Reactor Physics Towards a Sustainable Future," The Westin Miyako, Kyoto, Japan (September 28 - October 3, 2014 2014).
13. J. LEPPÄNEN, "Serpent - a Continuous-Energy Monte Carlo Reactor Physics Burnup Calculation Code," Accessed on http://montecarlo.vtt.fi/download/Serpent_manual.pdf (2015).
14. R. A. GRIMESEY, D. W. NIGG, and R. L. CURTIS, *COMBINE/PC-A Portable ENDF/B Version 5 Neutron Spectrum and Cross-Section Generation Program*, Idaho National Engineering Laboratory (February 1991).
15. X. S. LI and J. W. DEMMEL, "SuperLU_DIST: A Scalable Distributed-Memory Sparse Direct Solver for Unsymmetric Linear Systems," *ACM Trans. Mathematical Software*, **29**, *2*, 110–140 (June 2003).
16. Y. WANG, H. ZHANG, and R. MARTINEAU, "Diffusion Acceleration Schemes for the Self-Adjoint Angular Flux Formulation with a Void Treatment," *Nucl. Sci. Eng.*, **176**, 201–225 (2014).
17. E. E. LEWIS and W. F. MILLER, *Computational Methods of Neutron Transport*, John Wiley & Sons (1984).
18. S. SCHUNERT, Y. WANG, R. MARTINEAU, and M. D. DEHART, "A new mathematical adjoint for the modified SAAF-SN equations," *Annals of Nuclear Energy*, **75**, 340–352 (2015).
19. MOOSE FRAMEWORK AND MODULE DEVELOPERS, "MOOSE Wiki page," Accessed on http://mooseframework.org/wiki/ (2016).